THE ASTROPHYSICAL JOURNAL, 453:433–445, 1995 November 1

GIANT PULSES FROM THE CRAB PULSAR: A JOINT RADIO AND GAMMA-RAY STUDY

S. C. LUNDGREN,[1,2,3,4] J. M. CORDES,[3,4] M. ULMER,[5] S. M. MATZ,[5]
S. LOMATCH,[5] R. S. FOSTER,[1] AND T. HANKINS[6,7]
Received 1994 May 5; accepted 1995 May 8

ABSTRACT

The Crab Nebula pulsar emits bursts of radio emission as strong as 2000 times the average pulse amplitude. Using joint radio and gamma-ray observations of these giant radio pulses, we characterized intensity variations, measured absolute timing with 70 μs precision, and determined the spin-down model and interstellar dispersion. Fitting the flux-density histogram requires a two-component model—a narrow distribution of weak (but nonzero) pulses and a power-law component for giant pulses with an index of -3.3 and a low-intensity cutoff that is 33 times the mean of the weak pulses. The lack of time delay between giant pulses and weak pulses ($\Delta t = 6 \pm 12$ μs) suggests that the two emission mechanisms operate within a 4 km region. Daily changes in the apparent rate of giant pulses are caused by propagation effects in the interstellar medium (scintillation) rather than intrinsic variability of the giant-pulse mechanism. The distribution of time separations between giant pulses implies that the mechanism is a Poisson process. We interpret giant-pulse properties in the context of temporal-modulation and beam-waver models. Only the temporal-modulation model is consistent with the data. Empirical measurements place limits on the duration, size, and rate of temporal modulations in the magnetosphere.

Gamma-ray flux increases in the 50–220 keV range are limited to less than a factor of 2.5 concurrent with radio bursts. We discuss how the lack of gamma-ray variation constrains radio coherence mechanisms, the steadiness of electron-positron outflow, and the amount of inverse-Compton scattering of radio photons to gamma rays.

Subject headings: gamma rays: observations — pulsars: individual (Crab pulsar) — radiation mechanisms: nonthermal

1. INTRODUCTION

Giant radio pulses from the Crab pulsar were first detected shortly after its discovery (Heiles, Campbell, & Rankin 1970; Staelin & Sutton 1970). The Crab pulse profile consists of a main pulse, an interpulse 13 ms later, and at frequencies ≤ 600 MHz, a precursor component that precedes the main component by 2 ms (Counselman & Rankin 1971). Both the main pulse and interpulse exhibit the giant-burst phenomenon, but the precursor component does not (Gower & Argyle 1972; Argyle 1973). A long tail on the single-pulse flux-density histogram distinguishes the Crab fluctuations from all other pulsars. While other pulsars show a maximum intensity of 10 times the average, the Crab modulations span many orders of magnitude. Typical pulsars have Gaussian or exponential pulse-amplitude distributions (Backer 1971; Hesse & Wielebinski 1974; Ritchings 1976; Biggs 1986). For detectable individual pulses, the Crab pulse-amplitude distribution obeys a power law.

We undertook radio observations of giant pulses simultaneous with the *Compton Gamma Ray Observatory's* (*CGRO*) pointing toward the Crab in 1991 May. The purpose of our study was threefold. First, timing of radio pulses provided an accurate pulsar spin-down model for use in γ-ray data reduction. Second, the radio portion of this study collected the largest sample of giant pulses ever recorded. These 30,000 giant pulses allowed us to perform a comprehensive statistical analysis of giant-pulse phenomenology. Third and most important, concurrent radio and γ-ray observations afforded a unique opportunity to study correlations between the lowest and highest energy emissions from this young pulsar.

Finding a correlation (or lack thereof) between radio fluctuations and γ-ray emission has profound implications for models of the nature of young pulsar emission. Before examining these implications, we consider mechanisms for producing pulsar-intensity modulations on timescales of a few pulse periods to days. Two types of variability, diffractive and refractive scintillations, arise from propagation of the signal through the interstellar medium. After accounting for scintillation effects, the giant pulses remain, which suggests that they are caused by changes in the emission mechanism at the pulsar.

The multiwavelength portion of our study probes one aspect of pulsar emission theory: the relative roll of coherence variability versus pair-creation fluctuations in creating giant pulses.

Changes in pair-production efficiency would influence both radio and γ-ray emission. In contrast, improved radio coherence would have little or no effect on γ-ray emission. From our simultaneous observations of the Crab pulsar at γ-ray and radio wavelengths we find that the γ-ray emission remains unchanged during giant radio pulse emission. Hence, we conclude that radio coherence is the primary, if not the sole, mechanism for producing fluctuations in the radio emission. While we cannot rule out small changes in the γ-ray flux, and hence the pair-creation efficiency, we can set upper limits. These limits are discussed at the end of the paper.

[1] Remote Sensing Division, Code 7210, Naval Research Laboratory, Washington, DC 20375; lundgren@rira.nrl.navy.mil.
[2] National Research Council Research Associate.
[3] Astronomy Department, Cornell University, Ithaca, NY 14853.
[4] National Astronomy and Ionosphere Center.
[5] Department of Physics and Astronomy, Northwestern University, Evanston, IL 60208.
[6] New Mexico Institute of Mining and Technology, Socorro, NM 87801.
[7] National Radio Astronomy Observatories, Very Large Array, Socorro, NM 87801.

2. OBSERVATIONS

Radio observations were made with the Green Bank 43 m telescope 1991 May 15–27, using linearly polarized feed antennas at 1330 MHz for 2 days, at 800 MHz for 1 day, and at 812.5 MHz for 10 days. For data acquisition we used the NRAO Spectral Processor (SP) in a continuous sampling mode with real time dedispersion of a 20 MHz bandwidth across 256 channels. The dispersion smearing is reduced from 18 ms across 20 MHz at 800 MHz to 70 μs in the dedispersed sum of all channels. We sampled every 205 μs or 307.5 μs in hour-long scans 10 hr per day. The coarseness of our sampling was limited by the data-archiving rate onto magnetic tape combined with the large number of bits per data number. More than 12 bits are needed to give the dynamic range necessary to prevent saturation of the largest giant pulses. The complete data set includes over 10^7 pulse periods and 3×10^4 giant pulses.

The γ-ray observations were made by the *CGRO* Oriented Scintillation Spectrometer Experiment (OSSE) (Johnson et al. 1989), in the energy range from 50 to 220 keV. For pulsar observations, 1 ms sampling was used in event-by-event mode, in which each γ-ray photon is time tagged with 1.0 ms accuracy (Ulmer et al. 1991). OSSE observed the Crab 25% of the time over the 7 days included in this study. OSSE data overlapped with Green Bank data $\sim$2 hr spread throughout the 10 hr of radio observations per day, resulting in simultaneous observation of $\sim$3600 giant radio pulses.

3. CRAB PULSAR SPIN-DOWN MODEL

We developed analysis software to produce average pulse profiles and to extract giant pulses from the fast sampled data. In creating average profiles the program TEMPO (Taylor & Weisberg 1989) calculated the topocentric period behavior given input parameters for the observing time, pulsar period P, period derivative $\dot{P}$, and sky position. By cross-correlating average profiles with a high signal-to-noise ratio (S/N) template, we calculated precise pulse arrival times. The program TEMPO references these topocentric arrival times to the solar system barycenter. By fitting barycentric arrival times to a model, the program provides current values for P and $\dot{P}$. From the offset between 1330 MHz and 812.5 MHz arrival times, we fit for dispersion measure (DM) as well. An accurate DM is necessary to compare radio pulse arrival times (delayed by the interstellar plasma) to γ-ray arrival times (unaffected by dispersion). The Crab pulsar's DM varies on a monthly timescale by 0.2% due to motion of the supernova remnant surrounding the pulsar (Isaacman & Rankin 1977). Such fluctuations change the delay between radio and γ-ray pulses by up to 1.5 ms. Hence, an up-to-date value is required. The parameters in Table 1 resulted in a fit with rms residuals of 8 μs, holding all other parameters fixed to the known values (Taylor, Manchester, & Lyne 1993). The quoted DM accuracy allows conversion to infinite frequency arrival times to within 70 μs.

To form a complete picture of Crab pulse arrival times at several frequencies, we included data at 430 MHz and 1418 MHz from the Arecibo telescope, infrared data from the Palomar 5 m telescope (Lundgren, Cordes, & Beckwith 1995), and γ-ray data in our fit. The alignment of the pulse profiles is plotted in Figure 1. The infrared and radio alignment was calculated by correlating average profiles at each frequency to a common template and fitting barycentric arrival times to a spin-down model using the program TEMPO. The γ-ray arrival times are estimated by fitting a modified Lorentzian to the peak of the pulse profile and taking into account the 2.042144 s offset of the CGRO clock from coordinated universal time (UTC). All profiles are nearly aligned within the errors ($t_{IR} - t_{radio} = 70 \pm 70$ μs; $t_\gamma - t_{radio} = 500 \pm 250$ μs).

TABLE 1

CRAB PULSAR TIMING PARAMETERS

Parameter	Value
P	33.39207147394 ms
$\dot{P}$	$421.027597 \times 10^{-15}$ s s^{-1}
$\ddot{P}$	$-1{,}980{,}843. \times 10^{-30}$ s s^{-2}
Epoch.....	48,433.00 (MJD)
DM	56.776 ± 0.005 pc cm^{-3}

4. CALIBRATION OF RADIO DATA

The contributions to the radiometer temperature when observing the Crab pulsar are

$$T = T_R + T_{bg} + G \times [g_r(t) g_d(t) I_p(t) + I_{CN}] . \quad (1)$$

Each component must be measured to calibrate giant-pulse flux variability. Three effects combine to make the constant background signal—radiometer noise (T_R), background sky radiation (T_{bg}), and the Crab Nebula (I_{CN}). The amplitude of the pulsed portion of the signal, $I_p(t)$, is modulated by refractive and diffractive scintillations in the interstellar medium. We take these to be time-variable gains $g_r(t)$ and $g_d(t)$. The tele-

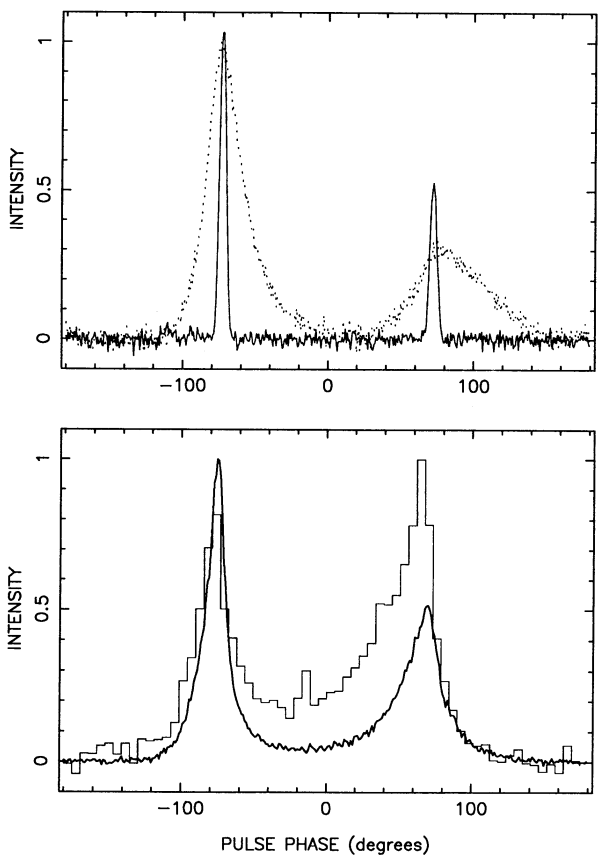

FIG. 1.—Radio and infrared (*upper panel: solid line and dotted line*, respectively) and γ-ray and X-ray (*lower panel: histogram and solid line*, respectively) profiles aligned with the measured timing offset after removing delay of the radio emission due to dispersion in the interstellar medium.

TABLE 2

RADIO CALIBRATION PARAMETERS

Parameter	Value
$T_R + T_{bg}$	47 K
I_{CN}	925 Jy
G	0.36 K Jy^{-1}
σ_T	13.5 Jy

scope gain is G. From observations of blank sky and the off-pulse level while pointed at the Crab pulsar and from the known flux density of the nebula at 800 MHz (I_{CN}), we determined $T_R + T_{bg}$ and G. Using the system temperature in equation (1) we estimate the noise level from $\sigma_T = T/(\Delta\nu\tau)^{1/2}$. The noise fluctuation level determines the minimum giant pulse distinguishable from noise. The results are summarized in Table 2.

Flux modulation due to diffractive interstellar scintillation is uncorrelated across frequencies larger than 100 kHz at 800 MHz for the Crab pulsar (Cordes, Weisberg, & Boriakoff 1985; Isaacman & Rankin 1977; Lyne & Thorn 1975). While substantial variability has been measured in the decorrelation bandwidth, 100 kHz is the maximum expected value at 800 MHz. For the 20 MHz bandwidth used in our data, the signal is summed over several independently modulated frequency bands, hence quenching the time variation of $g_d(t)$. Refractive scintillations, on the other hand, have a characteristic timescale of 2–5 days at 800 MHz (Rickett & Lyne 1990). This effect causes day-to-day variability $\approx 50\%$ of the average flux density, as seen in a plot of pulsed flux density for hour-long averages versus observation time (Fig. 2). In addition, this explains factor of 2 changes (on a timescale of days) in the rate of giant pulses exceeding a fixed threshold. Correlation of main-pulse with interpulse flux density provides further evidence that the variations are a propagation effect.

5. GIANT-PULSE RADIO PROPERTIES

While most individual pulses are too weak to detect (S/N = 0.07), single giant pulses may greatly exceed the noise

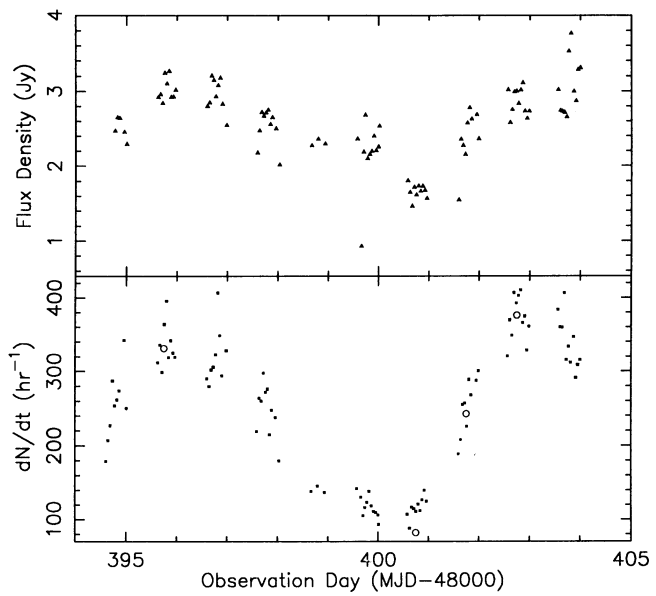

FIG. 2.—Variability in average flux density and rate of giant pulses exceeding the noise from day to day. Both variations are caused by RISS. The open circles plot the predicted number of giant pulses observed based on the fitted parameters of the power-law model (§ 5.1.1).

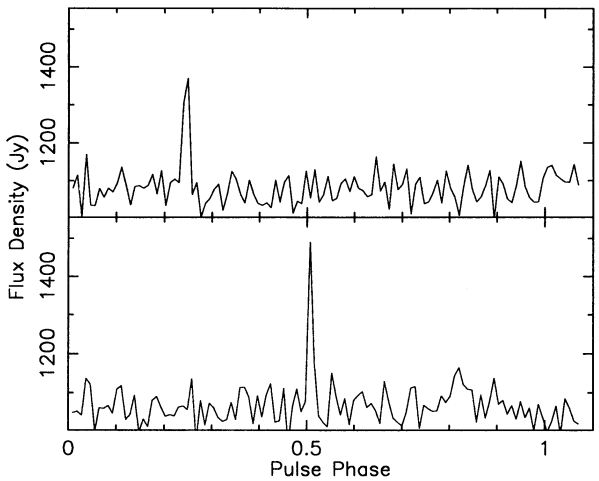

FIG. 3.—Single giant-pulse flux density at 800 MHz in upper (*upper plot*) and lower (*lower plot*) 10 MHz bands. The observed 9.2 ms delay was used to distinguish interference and random fluctuations from giant pulses. This giant pulse falls in the middle of the range of flux-density distribution. The difference in measured peak flux density is due to the unresolved pulse falling on a single time bin in the lower band and splitting between two bins in the upper band.

(Fig. 3). We compute the average flux density ("pulse energy" is often used in the pulsar literature, but we avoid this term), arrival time, and width for each giant pulse above the noise in our data. The flux density we use is averaged over a 1.5 ms window, large enough to include all significant emission. To convert to flux density averaged over the pulse period, this value is multiplied by the duty cycle 0.045. Data from other observations (Hankins & Rickett 1975) indicate that the true peak intensity can be significantly larger than what we observe, since some pulse widths are narrower than our time resolution by a factor of 3 or more.

To validate a giant pulse we require that it appear in both frequency bands and with the correct dispersion offset. We set a flux density threshold, $F_t = 120$ Jy $= 3\sigma_T$ in each channel, or 10% of the Crab Nebula's flux density (from Table 2), without introducing spurious giant pulses. With such a threshold and Gaussian-distributed noise, the probability of confusing a giant pulse with noise is 0.01 in a 1 hr observation, giving at most a few cases of noise confusion in the 10 days of observations.

One final method for eliminating interference from the giant pulses was to flag pulses with timing residuals larger than 1 ms. Such large residuals appeared only on days with particularly strong radio frequency interference (RFI). Hence, we attributed them to the RFI. Only 1.5% of the giant pulses were eliminated by this criterion.

To develop a complete picture of giant-pulse emission, we undertook a detailed examination of the amplitude, rate, time separation, widths, and arrival times of giant pulses. Our amplitude analysis in § 5.1 provides convincing evidence for two distinct emission modes. The remaining sections provide the observational results necessary to develop models for the emission mechanism. In §§ 6.1 and 6.2 we consider the merits of two possible models—one in which emission is temporally modulated and another in which the beaming angle of the emission changes from one period to the next.

5.1. *Pulse-Amplitude Distribution*

To quantify variability in the radio emission and compare with measurements at other frequencies, we calculated an

average fluctuation profile, $\langle I_{\rm RMS}(\phi)\rangle = [\langle I^2(\phi)\rangle - \langle I(\phi)\rangle^2]^{1/2}$, for phase ϕ. The modulation index ($\langle I_{\rm RMS}(\phi)\rangle / \langle I(\phi)\rangle$) is determined by a combination of the intensity distribution of giant pulses and the amount of pulse phase jitter relative to the pulse width. Typically for the Crab pulsar, the modulation index is near unity. Most of this modulation comes from giant pulses. In fact, in several of our 1 hr averages, a single giant pulse of 400 times the average increases the modulation index to ~ 8. By contrast, optical measurements (Hegyi, Novick, & Thaddeus 1971) place an upper bound of 1% on pulse-to-pulse fluctuations. More recent *Hubble Space Telescope* ultraviolet and optical observations detected no correlation in fluctuations from pulse to pulse, although no upper limit on fluctuations above counting statistics is quoted (Percival et al. 1993). Our own infrared data (Lundgren et al. 1995) limit variability to $< 1\%$ as well. In the gamma-ray data, substantial variability and uncertainty in the background count rate make a meaningful calculation of modulation index impossible.

The modulation index alone does not capture the full extent of giant-pulse variability. In fact the value of unity for the Crab pulsar is comparable to that for many other radio pulsars (Backer 1973; Bartel, Sieber, & Wolszczan 1980; Weisberg et al. 1986). To capture the uniqueness of Crab emission, we must study individual giant pulses, rather than simply the average behavior.

5.1.1. *Pulse-Amplitude Distribution—Fit*

The flux-density distribution is displayed in Figure 4 for giant pulses meeting our RFI-rejecting criteria. Three striking features are exhibited. The log-log plot in the figure clearly demonstrates the power-law tail spanning an order of magnitude in flux. The tail is well represented by $N_{F_\nu} \propto F_\nu^{-\alpha}$ with $\alpha = 3.46 \pm 0.04$ for $F_\nu > 200$ Jy, where N_{F_ν} is the number of pulses within a 5 Jy range of F_ν. The sharp cutoff for $F_\nu < 125$ Jy corresponds to $F_\nu = F_t$. However, the roll-off at 125 Jy $< F_\nu < 200$ Jy represents the intrinsic amplitude distribution rather than an artifact of our sampling method. Initially, we believed that the roll-off was an incompleteness effect near F_t. A large fraction of pulses barely exceeding the threshold in one frequency band might be excluded because they fall just short of the threshold in the other frequency band. However, changing F_t did not affect the roll-off. We were forced to conclude that the roll-off is a feature of the pulse-amplitude distribution.

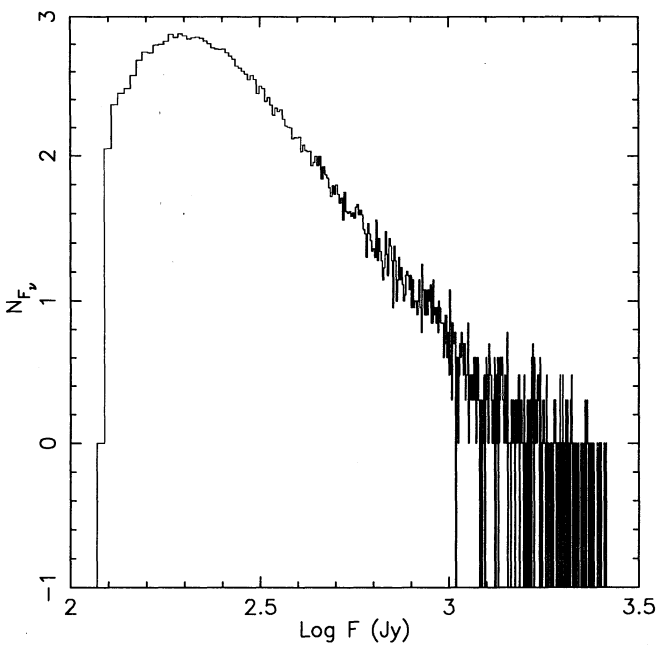

FIG. 4.—Distribution of giant-pulse flux densities is displayed in a log-log plot. The average flux density of 2 Jy is off the scale of the plot. Each bin contains the total number of pulses observed within the corresponding 5 Jy flux-density range.

To confirm this hypothesis, we undertook a more comprehensive analysis of the giant-pulse amplitude distribution. From each day's data we generated a histogram of main-pulse flux density for *all* periods—both giant *and* weak pulses. Only 4 days of data were usable for this portion of the study. The other data were corrupted by low-level RFI that altered the flux-density distribution in the region of interest near the roll-off. By fitting a Gaussian to the off-pulse amplitude distribution of 1 day's data, we could identify days where RFI was present and reject data from those days. For each of the 4 good days, we fitted the data to a model amplitude distribution convolved with Gaussian noise.

First, we tried the simplest assumption: observed giant pulses are the tail of a continuous distribution of pulse intensities. In the simplest manifestation of such a model, the observed power-law distribution (for $F_\nu > 200$ Jy) extends to $F_\nu < 200$ Jy with the same index: $\rho_F(F_\nu) \propto F_\nu^{-\alpha}$ for $F_\nu > F_c$, where $\rho_F(F_\nu)$ is the probability density function (p.d.f.) for a giant pulse at flux density F_ν. The low-amplitude cutoff (F_c) of the power-law distribution is fixed by normalization and the fraction of pulses observed with $F_\nu > 200$ Jy and hence is not a free parameter. Considering the roll-off at low amplitudes noted earlier, we believed such a model would not fit the data. The upper plot in Figure 5 shows the observed distribution plotted with the model distribution convolved with Gaussian noise. For $F_\nu < 200$ Jy the fit is poor, as expected. Extending the power-law distribution to lower flux densities gives too many giant pulses in the range 10 Jy $< F_\nu < 200$ Jy. To reduce this excess some of the pulses must be shifted from here to much lower flux densities.

To improve the consistency of our model with the distribution below 200 Jy, we propose that only a fraction (f) of the pulses fall in a power-law distribution. The remaining, weaker pulses fall on a distribution peaked at a flux density (F_w) significantly below the power-law cutoff (F_c). For simplicity, we model the distribution of weak pulses as a Dirac delta function. Such a model minimizes the number of parameters while still containing all of the major features of a more general distribution. It excludes parameters for a range of low-intensity pulses and a more gradual cutoff of the power law at low flux density. We have not included a high-amplitude cutoff, because there is no evidence for one in the data. The p.d.f. we have constructed can be represented as

$$\rho_F(F_\nu) = \begin{cases} (1-f)\delta(F_\nu - F_w) & \text{if } F_\nu < F_c \\ CF_\nu^{-\alpha} & \text{if } F_\nu > F_c \end{cases}, \qquad (2)$$

where $C = f(\alpha - 1)F_c^{(\alpha-1)}$, from normalization. To compare with the observed amplitude distribution, the model $\rho_F(F_\nu)$ is convolved with a Gaussian of width determined by the off-pulse noise σ_F.

Initially, we allowed four of the five fit parameters to vary: f, α, F_w, and F_c. We fixed the width of the Gaussian to σ_F. We

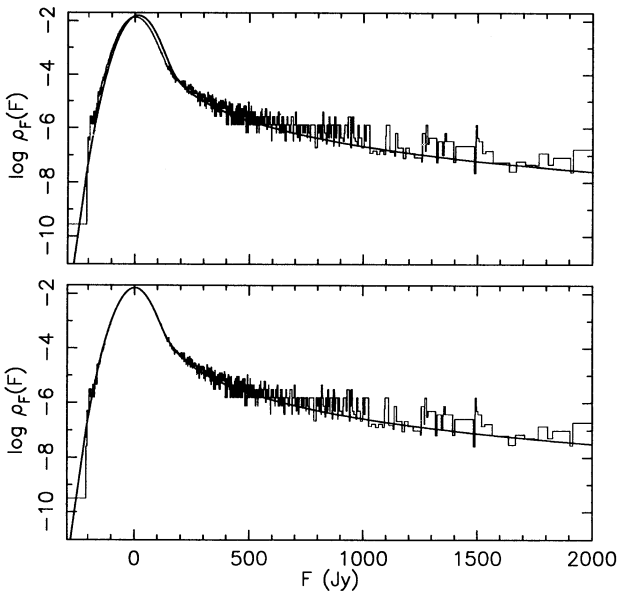

FIG. 5.—Giant-pulse/weak-pulse flux-density distribution and fits. The upper fit is an extrapolation of the power law ($\alpha = 3.3$) at high fluxes to low enough energies to include all pulses and convolved with Gaussian noise. Since this fit exceeds the data at low flux densities, it suggests that the giant-pulse distribution has a higher cutoff at low flux densities, and hence two distributions are needed–one for weak pulses and a power law for giant pulses. The lower fit assumes an intrinsic distribution containing weak pulses at a fixed low flux $F_w = 1.4$ Jy and giant pulses in a power law with index $\alpha = 3.3$ and low-amplitude cutoff $F_c = 51$ Jy. The intrinsic distribution is convolved with Gaussian noise of σ calculated from the off-pulse noise. For this fit $\chi^2/N = 0.95$. Negative flux pulses come from random noise fluctuations.

derived the best-fitted parameters by minimizing χ^2,

$$\chi^2 = \sum_j \left(\frac{\rho_{dj} - \rho_{fj}}{\sigma_{dj}} \right)^2 , \quad (3)$$

where ρ_{dj} and ρ_{fj} are probability densities of the data and the fit at each flux density j and σ_{dj} is the Poisson error in each bin of the observed distribution.

The lower plot in Figure 5 shows the fit for a single day of data. The fitted parameters for each day are summarized in Table 3. The values of χ^2/N near unity imply the model is a good representation of the data. In addition, the residuals show no systematic deviations of the model from the data, even for $F_v < 200$ Jy, where the simpler model failed. The giant-pulse p.d.f. has a power-law index of 3.3 with a low-energy cutoff F_c that varies from 30 to 60 Jy. The *giant* pulses make up 2.5% of all pulses. This fraction exceeds the number actually observed, because $F_c \ll F_t = 120$ Jy. The remaining *weak* pulses fall on a delta function at flux density ranging from 0.8 to 2.1 Jy. Although the power-law slope and pulsed fraction vary 5 times more than the measurement error estimated in each fit, small daily variations in these values can be attributed to low-level interference.

TABLE 3

PARAMETERS OF GIANT-PULSE FLUX DISTRIBUTION

Date	α	f	F_w (Jy)	F_c (Jy)	χ^2_r	Average Flux (Jy)
May 19.....	3.36	0.0238	2.13	63.	0.917	3.06
May 24.....	3.30	0.0285	0.83	31.	0.984	1.65
May 25.....	3.30	0.0270	1.43	51.	0.948	2.4
May 26.....	3.06	0.0229	1.92	60.	1.020	2.8
Errors.....	0.03	0.0010	0.07	1.	0.002	0.1

To place an upper bound on the true width of the weak pulse amplitude distribution, we allowed its width to vary. The delta function at F_w still gave the best fit. A 1 σ error allows a width up to $3F_w$ (a few bins of our histogram), significantly less than F_c. This test clearly demonstrates the bimodality of the distributions.

5.1.2. *Pulse-Amplitude Distribution—Discussion*

Some important features of these fits require further discussion and clarification. As seen in Table 3, F_w and F_c vary significantly from day to day. These variations are correlated with the observed day-to-day variability of the average flux density due to refractive interstellar scintillation (RISS). The effect of RISS is to increase or decrease each giant pulse by the same proportion.

The effect of RISS on the distribution $\rho_F(F_v) = CF_v^{-\alpha}$ is a time-variable scale factor and cutoff: C becomes $Cg_r(t)^{-\alpha}$ and F_c becomes $F_c\, g_r(t)$. Similarly for the weak pulses F_w becomes $F_w\, g_r(t)$.

As seen in Table 3, F_w and F_c vary in proportion to the average flux density. The fact that both parameters vary as expected, while the giant-pulse rate (f/P) remains constant, provides a strong consistency check on the model. We conclude that the nonzero flux density of weak pulses and the break in the distribution between weak and giant pulses are features of the pulse-amplitude distribution and not artifacts of interference.

Comparison of our results at 800 MHz with those measured earlier at 146 MHz (Argyle & Gower 1974) yields spectral information about the giant pulse amplitude distribution. We need to add 1 to the slope of our differential distribution to compare with the earlier measurement of the cumulative distribution. The -2.3 slope of the distribution measured at 800 MHz is consistent with the -2.5 power-law index at 146 MHz, within the uncertainty in the earlier measurement. However, at low frequencies no distinction can be made between weak pulses and giant pulses. They all fall on a single power law. In addition, we find at least 40 times more pulses ($f = 0.025$) above the fitted cutoff (F_c) at 20 times the average amplitude than are found at 146 MHz ($f = 0.0006$). Another way of looking at the comparison is that 0.025 of the pulses are 5 times stronger relative to the mean at 800 MHz than at 146 MHz. Our interpretation is that if individual giant pulses are broadband, then weak pulses must have a steeper spectrum than strong pulses. Alternatively, if individual giant pulses are narrowband (~ 100 MHz or less), then the rate of the strongest giant pulses must increase with frequency between 146 MHz and 800 MHz. Distinguishing these possibilities will require future simultaneous dual-frequency observations of giant pulses to determine the bandwidth of individual giant pulses.

In order to explore the high-amplitude extent of the power-law distribution, we calculated the amplitude of the largest pulse we would expect to find in the 2 week duration of our observations. We find from extrapolation of the $\alpha = 3.3$ power law that there would be two giant pulses above $1700\langle F_v \rangle$. In fact there are two: one at $1900\langle F_v \rangle$ and one at $2000\langle F_v \rangle$. There is a 20% chance that the highest observed flux density is $2000\langle F_v \rangle$, as we measured. From these results, we conclude that we are not seeing a high-intensity cutoff of the distribution in our 2 weeks of observations.

The best test of our bimodal model for giant-pulse flux density is to probe the low-intensity portion of the distribution, dominated by noise in our data. Such a study would be possible using VLA observations in phased array mode. In that mode, the effective beam size is a few percent of the nebula angular size, thus resolving out most of the nebular background. With the noise then dominated by the system temperature, signal-to-noise ratios of 10 times that at the Green Bank 43 m telescope are possible. Confirming bimodality would then be feasible.

The bimodal distribution we have found suggests weak pulses and giant pulses may result from quite different emission processes, possibly even different emission regions in the magnetosphere. To explore this possibility further, we studied some of the other radio properties of giant pulses.

5.2. *Giant-Pulse Rate*

To model the time distribution of giant pulses, we postulated that each giant pulse is independent of every other giant pulse. In such a Poisson process, we expect an exponential distribution of time separations. Rotation of the pulsar beam through our line of sight samples the Poisson process at discrete intervals determined by the period. Sampling an exponential distribution at fixed intervals gives an exponential distribution. Perfect exponential drop-off of the observed distribution (Lundgren 1994) from one to 2000 periods confirms the Poisson nature of giant-pulse emission.

For giant pulses exceeding our 125 Jy threshold, we estimate a rate of $1/\Delta\tau_{sep} = 0.0783 \pm 0.0006\ s^{-1}$, or one giant pulse every 383 periods. The *observed* rate of giant pulses (dN/dt) above a fixed threshold (F_t) changes from day to day (Fig. 2), whereas the rate of all giant pulses (f/P) remains fixed (Table 3). The observed variability is a selection effect resulting from RISS. As argued in the previous section, the amplitude distribution shifts from day to day because of RISS, thus shifting some giant pulses above or below our threshold. We use the parameters of the p.d.f. from Table 3 to calculate the observed rate of giant pulses for each of the four r.f.i.-free days. To calculate the fraction of pulses exceeding F_t, we integrate the shifted power-law distribution,

$$f_o = \int_{F_t}^{\infty} dF \rho_F(F) * \rho_N(F) , \qquad (4)$$

where the asterisk denotes convolution with Gaussian noise $\rho_N(F)$. Figure 2 shows the predicted fraction of pulses exceeding F_t and the actual fraction of pulses observed. The good agreement provides further support for the quality of the power-law model with a cutoff. To convert the observed rate to an intrinsic rate (for an observer corotating with the pulsar), we need to know the typical intrinsic duration of giant pulses.

5.3. *Giant-Pulse Widths*

Figure 6 displays a histogram of observed widths for validated giant pulses. The width is the equivalent width calculated by integrating the flux density in four radio-frequency channels and dividing by the sum of the peak flux density in each channel. The measured width for single pulses is limited by our coarse time samples. The measurement is further confused by the dispersion between the four frequency channels. However, the shape of the distribution of equivalent widths reflects the true pulse widths, even for true widths narrower than our sampling interval. A narrower pulse is split between two bins less often than a broad pulse, hence giving a narrower distribution of equivalent widths.

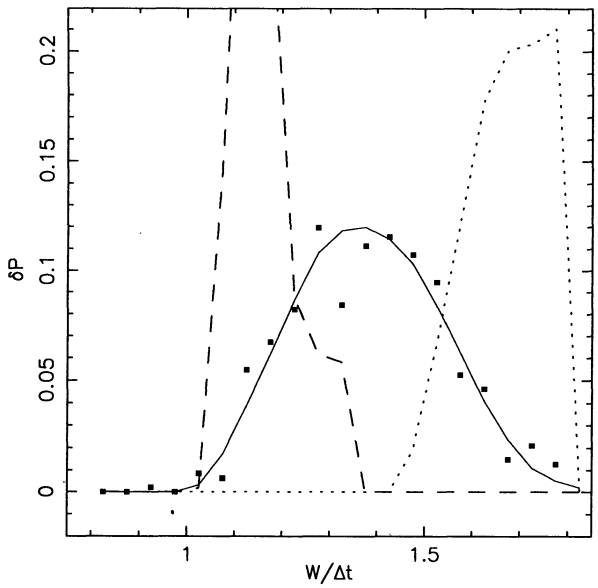

FIG. 6.—Predicted (*lines*) and measured (*filled squares*) pulse-width distribution in units of the sample interval $\delta t = 205\ \mu s$. The predictions from left to right assume intrinsic widths of ($20 < w < 40\ \mu s$), ($40 < w < 120\ \mu s$), and ($120 < w < 180\ \mu s$).

We conducted a simulation to estimate the true pulse width. We used a giant-pulse shape with an instant turn-on followed by an exponential decay convolved with a 70 μs rectangle function for the dispersion across one frequency bin. We adjusted the exponential decay to give the best fit to the equivalent width distribution and allowed for a small range of widths. By allowing the phase of the giant pulse to vary with a uniform distribution across the sample interval of the first channel and calculating the effect of dispersion and binning on the measured amplitude in the other channels, we simulated the observations. The width histogram from the giant-pulse data is fitted well by using an intrinsic e-folding width $w_{gp} = 100\ \mu s$, as seen in Figure 6.

To probe the detailed shape of the giant pulses, data with much higher time and frequency resolution are needed, since the estimated pulse width is half our shortest sample interval and comparable to the dispersion smearing across one channel. Hankins (1993) made high time-resolution observations at the Very Large Array (VLA). Preliminary results resolve giant-pulse fine structure into multiple 10 μs spikes at 1400 MHz. Earlier work determined a 90 μs exponential decay timescale for spike flux density at 430 MHz (Hankins & Rickett 1975) that is attributed to interstellar scattering. Our lower resolution measurements seem to be in agreement with these earlier measurements to within a factor of 2, considering that the 800 MHz width would fall between the two earlier measurements.

5.4. *Giant-Pulse Arrival Times*

The large sample of giant-pulse arrival times allows a precise measurement of the delay between giant-pulse arrival times and average-profile arrival times (dominated by weak pulses). We calculated arrival times for individual giant pulses, simply referencing the time to the bin number of the pulse. The residuals from fitting the arrival times to the spin-down model

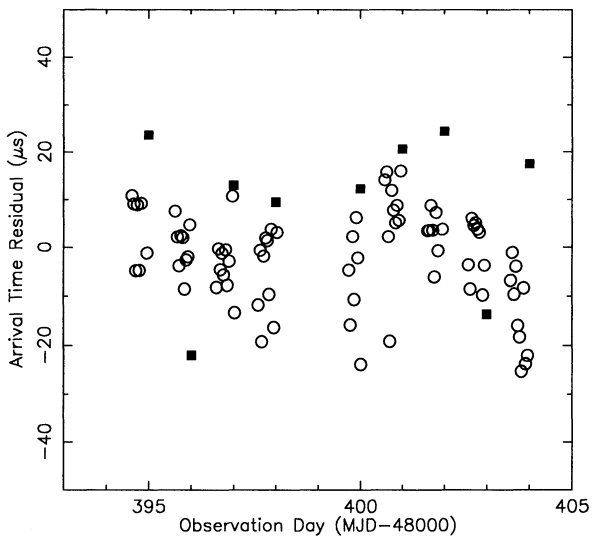

FIG. 7.—Residuals for 1 hr average-profile (*circles*) and average giant-pulse (*squares*) arrival times from a fitted pulsar spin-down model. No significant offset is measured between giant-pulse and average-pulse arrival times.

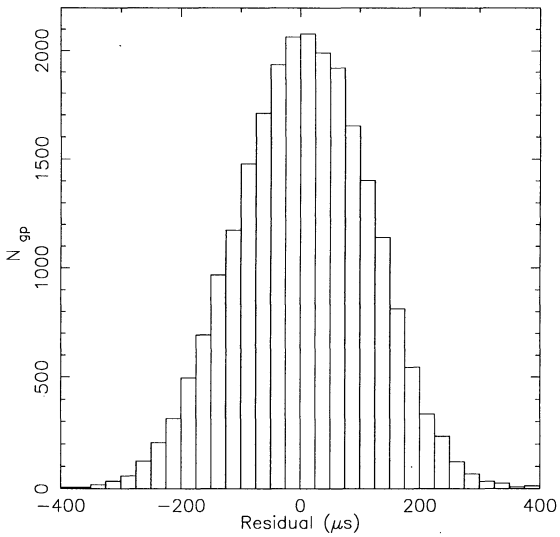

FIG. 8.—Histogram of giant-pulse arrival time residuals. The histogram is formed from the residuals from the spin-down model for all giant pulses observed.

are shown in Figure 7. The average offset between the giant pulses and the average pulses is 6.6 ± 7.4 μs—consistent with no offset.

Since our measurement of zero offset contradicts an earlier measurement of an offset in 430 MHz observations (Friedman & Boriakoff 1990), we have recalculated the offset in the same way as the earlier measurement. On days with low RFI, we calculated subaverage profiles of only giant pulses within specified energy ranges. We aligned each of these giant-pulse average profiles with the same template used for the overall averages to estimate arrival times. We fitted these arrival times using TEMPO and calculated the average offset (δt) between the giant-pulse averages and the overall averages. For the smallest giant pulses we measure $\delta t = 6 \pm 12$ μs. For the largest giant pulses we measure $\delta t = 32 \pm 20$ μs. For middle range giant pulses we measure $\delta t = 10 \pm 9$ μs. The errors here are estimated from the variation in offset from one hour average to the next. A positive offset implies later arrival.

Our errors imply we would have seen the -70 μs offset quoted in earlier work (Friedman & Boriakoff 1990). Perhaps the arrival-time estimates at 430 MHz are influenced by the presence of the precursor pulse in the average profile and the absence of it in the giant-pulse subaverage profile. Alternatively, perhaps the number of giant pulses found in the earlier study (1000) was insufficient to provide a stable average profile or the profile-alignment method of generating a high S/N profile introduced a bias between the giant-pulse average and the overall average.

5.5. *Pulse Phase Jitter*

Pulse arrival-time measurements provide a further test for giant-pulse emission models. Using the overall histogram of giant-pulse arrival-time residuals from the spin-down model (Fig. 8) we can extract information about pulse phase jitter. Such jitter can be caused by changes in the location of the emission region in the magnetosphere (either height or angular changes) or by turning on or off the emission in the middle of the time the beam is aligned with our line of sight. The contributions to the residuals from the 307 μs sample interval ($\sigma_{\rm samp}$) and the 70 μs dispersion smearing ($\sigma_{\rm dm}$) add in quadrature with the jitter (expressed as a fraction of pulse width: $\eta = \sigma_{\rm jit}/w_{\rm gp}$) to give the total observed spread in residuals ($\sigma_{\rm toa}$). We can solve for the jitter as a fraction of the intrinsic pulse width

$$\eta w_{\rm gp} = (\sigma_{\rm toa}^2 - \sigma_{\rm samp}^2 - \sigma_{\rm dm}^2)^{1/2} . \quad (5)$$

Using $\sigma_{\rm toa} = 130$ μs from the histogram, $\sigma_{\rm samp} = 89$ μs, and $\sigma_{\rm dm} = 20$ μs gives $\eta = 0.9$ for $w_{\rm gp} = 100$ μs, comparable to values seen in other pulsars.

6. THEORETICAL IMPLICATIONS OF OBSERVED GIANT-PULSE PROPERTIES

By combining our empirical measurements of giant-pulse properties into one coherent picture, we can extract information about the temporal modulation and angular beaming of the emission as observed from the corotating frame of the pulsar. We focus on particular measured properties, including the single-pulse width $w_{\rm gp}$ (§ 5.3), the average-pulse width $w_{\rm ave}$ (Fig. 1), the time separations $\Delta\tau_{\rm sep}$ (§ 5.2), and the single-pulse arrival-time residuals $\Delta\tau_{\rm res}$ (§ 5.4). The quantities constrained in our model include the average, $\theta_{\rm ave}$, and instantaneous, $\theta_{\rm inst}$, angular size of the emission region, the characteristic times for the pulsar emission to be in the high state $t_{\rm hi}$ and the low state $t_{\rm low}$, and the characteristic separation between giant pulses $t_{\rm sep} = t_{\rm hi} + t_{\rm low}$. Figure 9 depicts the definition of the three characteristic times. The angular sizes can be converted to times by multiplying by the pulse period P, which gives the time for the region to rotate through our line of sight.

The data provide two windows on the intrinsic behavior. The pulse-width analysis probes short-timescale (100 μs $< \Delta t <$ 0.5 ms) behavior, limited by our time resolution and the sweep time for the beam to pass through our line of sight. The time separation analysis, on the other hand, probes long-timescale behavior (>1 period). While they do not provide a complete picture, together the two windows yield much insight into the problem.

We examine the issue from two perspectives. The first perspective assumes that the observed amplitude variability is due to temporal modulation of the emission that would be seen in the corotating frame of the pulsar. The strong emission turns

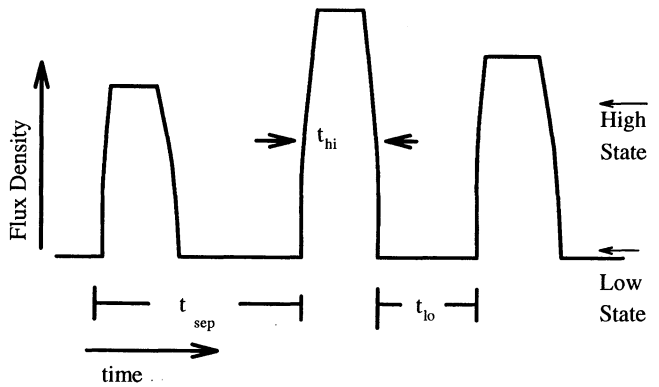

FIG. 9.—Definitions of temporal-modulation parameters t_{sep}, t_{hi}, and t_{lo}, the intrinsic separation between high states, duration of high states, and duration of low states, all as measured by a corotating observer

on for a characteristic length of time t_{hi} and with a characteristic rate $1/t_{sep}$. It further assumes that the beam is locked to a fixed position in rotational phase by the magnetic field (at least within the one pulse-width jitter typical of all pulsars). Thus, whenever the giant-pulse mechanism is active while the average beam points toward us, we see it. This contrasts with the second perspective in which rotational phase lock of the beam is lost because of magnetic field instabilities (Arons 1981). In this situation the strong narrow beam may be on continuously but aligned with Earth's line of sight only during occasional pulse periods. In other pulse periods, the angle of the beam direction from Earth's line of sight is larger than the beam angular width. In this scenario both the fraction of observed pulses that are giant and the amplitude variability are determined by the width of the beam and by the amount the beam wavers. In the next two sections we will see that only the temporal-modulation model is consistent with the observations.

6.1. *Temporal Modulation*

In the temporal-modulation model we discuss three ranges of possible values for t_{hi}:

$$t_{hi} > P\,, \tag{6}$$

$$P\theta_{ave} \lesssim t_{hi} < P\,, \tag{7}$$

$$t_{hi} \ll P\theta_{ave}\,, \tag{8}$$

where P is the pulsar spin period. The first and last possibilities are ruled out by our data.

Equation (6) is excluded by the observed distribution of time separations τ_{sep} (§ 5.2). If t_{hi} were longer than one period, the fraction of giant pulses separated by one period would exceed the prediction for a Poisson process. Taken to the extreme, if $t_{hi} \gg P$, then every observed giant pulse would come in a cluster. The data show quite the opposite. Since no excess at one period is observed, the upper bound on t_{hi} is one period (33 ms). Further proof that there is no memory of giant-pulse behavior spanning adjacent pulse periods comes from a comparison of pulse-amplitude p.d.f. for pulses immediately following giant pulses with the same plot for all pulses. There is no significant difference between the curves (Fig. 10), implying there is neither correlation nor anticorrelation of intensity from pulse to pulse. The apparent short duration of giant bursts is in sharp contrast to mode changing and pulse nulling seen for other pulsars (Deich et al. 1986) in which the two intensity states each last many pulse periods.

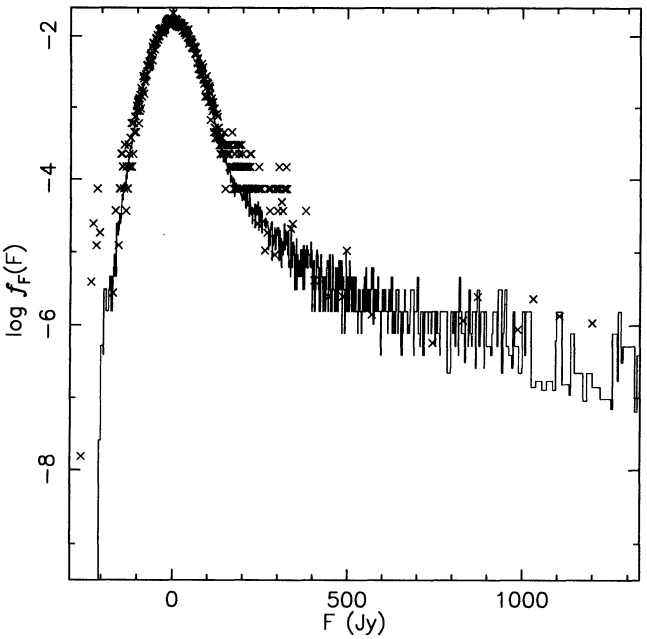

FIG. 10.—Comparison between pulse flux distributions including all pulses and including only pulses preceded by giant pulses (*crosses*). The agreement suggests giant-pulse flux is not correlated over timescales of one period. For correlation/anticorrelation the distribution of the crosses would exceed/remain below the all-pulse distribution for large flux densities.

Equation (8) can be eliminated by comparing the observed values of $\Delta\tau_{res}$ with w_{gp} and w_{ave}. To make the argument, we consider the relation between the intrinsic properties and the empirical measurements. If equation (8) holds, $w_{gp} \sim t_{hi}$. The rotation is too slow to rotate the entire emission region through our line of sight before the emission returns to the low state. Hence, the observed *single*-pulse width is determined by the high-state duration. On the other hand, the *average*-profile width w_{ave} and the spread of arrival time residuals $\Delta\tau_{res}$ will reflect the full angular size of the emission region ($w_{ave} \sim \Delta\tau_{res} \sim P\theta_{ave} > t_{hi}$). However, we found quite the opposite in § 5.5. The jitter is comparable to the single-pulse width, implying that $t_{hi} \gtrsim P\theta_{ave}$.

Under the condition of the remaining possibility (eq. [7]), the time-separation distribution (§ 5.2) limits the allowed values for t_{hi}, t_{sep}, and θ_{inst}.

The observed giant-pulse rate measured in § 5.2 comes from sampling the emission once per period. In a given rotation period, the probability of seeing a giant pulse is $p_1 = (t_{hi} + P\theta_{inst})/t_{sep}$. The probability of seeing a given number of periods ($n = t/P$) *between* observed giant pulses is given by the binomial distribution $(1 - p_1)^n p_1$. We can approximate this by a Poisson distribution in the case in which $p_1 \ll 1$: $p(n) = p_1 e^{-np_1}$.

Hence, fitting the distribution of observed time spacings between giant pulses gives the ratio

$$f = p_1 = \frac{P\theta_{inst} + t_{hi}}{t_{sep}}\,. \tag{9}$$

We have related the measured fraction of pulses that are giant (f) to the ratio of parameters measured by a corotating observer.

We consider the two extreme cases allowed by equation (7). In the first case, t_{hi} is comparable to the angular sweep time.

Both the high-state duration and the angular beam size must be comparable to the measured width in this case. This amounts to a special case of equation (9), where $t_{hi} \approx P\theta_{inst} \approx w_{gp} = 100$ μs. For giant pulses above 125 Jy, $t_{sep} = 76$ ms. Using the fit of flux density distribution, where all giant pulses exceed 50 Jy, $t_{sep} = 8$ ms. This places an upper limit on the rate of giant pulses.

In the other case, the high-state duration is much longer ($t_{hi} \gg P\theta_{inst}$), and the observed width is the angular size ($w = P\theta_{inst}$). Since the first term in equation (9) is insignificant, we measure the fraction of time spent in the high state t_{hi}/t_{sep}. For giant pulses above our 125 Jy threshold, $t_{sep} = t_{hi}/f = (380 \pm 50)t_{hi}$. Instead, using the full fit of flux density distribution in § 5.1.1 ($f = 0.025$, $F_c = 50$ Jy), we have $t_{sep} = (40 \pm 3)t_{hi}$. The extreme value, $t_{hi} \approx P = 33$ ms, gives a lower limit on the rate of giant pulses, $t_{sep} = 12$ s for giant pulses above 125 Jy or $t_{sep} = 1.3$ s for the fit of all pulses. We note that a duration that happens to be a substantial fraction of one period would not be purely fortuitous. The timescale for a relativistic particle to travel through the magnetosphere to the light cylinder is on the order of P/π.

The above measurements place constraints on magnetospheric emission models. We consider a model in which the giant pulses arise from cylindrical flux tubes in the polar cap region. We let h, Δh, and d be the height, length, and diameter of the tube, as depicted in Figure 11. Let Δr be the distance traveled while the high-state emission is activated. Causality implies that $\Delta h/c < t_{hi}$. From geometry we know $d/h < \theta_{inst}$. The observed single-pulse width results from a combination of d, Δh, curvature of the field lines, and the $1/\gamma$ opening angle of the radiation from individual particles. Considering parameters separately, the $w_{gp} = 100$ μs width places a lower limit on γ of $\gamma \geq P/(2\pi w) = 50$ for the particles participating in the emission. If $\Delta r > \Delta h$ then $t_{hi} = \Delta r/c$. As stated earlier, even emission out to the light cylinder gives only $\Delta r \sim Pc/\pi$. The lower limit on t_{hi} gives $r > 30$ km.

6.2. *Fluctuations in Angular Beaming*

The second perspective assumes that giant pulses come from steady emission in an extremely narrow pencil beam. We observe a giant pulse only when magnetospheric currents alter the beaming direction, aligning the beam with our line of sight.

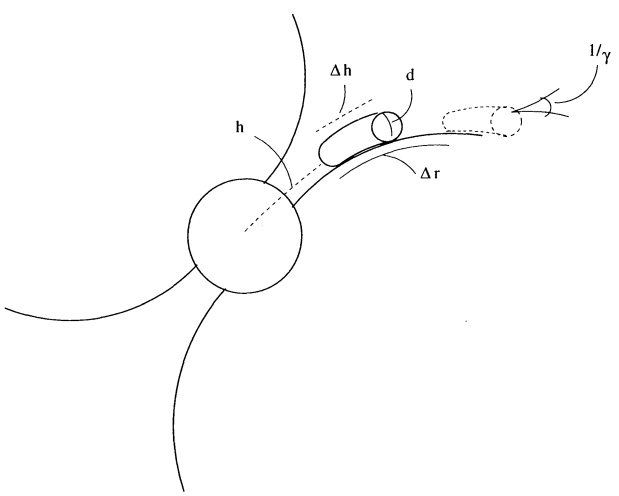

FIG. 11.—Giant-pulse emission diagram. Here we label the dimensions relevant to a flux-tube model for giant-pulse emission.

Since giant pulses show no periodicities and no preferred spacings and behave like a Poisson process, any wobble would have to be a random process. Each of the parameters in the earlier model has an analogous parameter in this model. What we previously called "duration" now corresponds to the amount of time the beam stays closely aligned with our line of sight. This in turn is determined by the angular speed of the wobble and the angular size of the beam. The characteristic time t_{sep} now refers to the average time between alignments with our line of sight. The angular size remains unchanged.

Once again the arrival-time residuals (Fig. 8) and jitter (§ 5.5) can provide insight into this model. Now the spread of the arrival times is determined by the extent of the beam wobble along the path of the line of sight (i.e., in the direction of the pulsar's equator). We saw in the previous section that the residual spread is comparable to the measured width of the beam. That means the beam width is comparable to the maximum wobble along the line of sight. The only way this could be reconciled with the small fraction of pulse periods that are giant is if the extent of wobble perpendicular to the pulsar's equator is significantly larger than that along the equator. For such a model to match the rate of observed giant pulses (one out of 40 using the lower threshold of the fitted model), the extent of perpendicular wobble would have to be 40 times that parallel to the line of sight path—45°. Such a geometry violates the inherent symmetry of the pulsar for any slice of the line of sight across the wobble region.

6.3. *Implications of Arrival-Time Residuals*

Our 10 μs limit on the offset between giant-pulse and weak-pulse emission constrains the spatial relation between the emission regions. Lack of an offset suggests that while the emission *mechanism* may be different for giant and weak pulses, the emission *region* is the same for both, within 3 km. Alternatively, the beam geometry and emission height could conspire to make the phases agree by chance, although the added complexity makes this possibility less appealing.

The temporal-modulation model for giant-pulse production predicts that in the case in which t_{hi} is much longer than the measured pulse-width resolution, there should be a correlation between timing residuals and both width and flux density measured. For large negative residuals, there should be an excess of low-amplitude, short-duration pulses that are observed just before they shut off. Similarly, for large positive residuals, there will be an excess of low–flux-density, short pulses that are observed just as they turned on. For small magnitude residuals, we expect large-amplitude pulses that are turned on for the full amount of time we can observe them. For the beaming-fluctuation model for giant pulses, no correlation would be observed. The beaming fluctuations would cause arrival-time jitter independent of measured width or flux density.

Our data show no correlation between arrival-time residual and pulse width. This would seem to favor the beaming model, which we have already ruled out in the previous section. However, a number of effects conspire to make the correlation impossible to detect in our data. Since $w_{gp} \sim t_{sample}/3$, the short-duration pulses described above have a poorly sampled arrival time. Large-number statistics might overcome the poor sampling. However, then the steepness of the power-law amplitude distribution makes the average flux-density estimate at each arrival-time residual too uncertain to see any trend. We would see the effect with 30 μs sampling. Another necessary

improvement is to probe deeper into the noise to detect more of the smaller giant pulses. Perhaps the giant pulses on the edge of the detection window are mostly hidden below our noise threshold.

7. CORRELATION BETWEEN RADIO AND γ-RAY DATA

A primary goal of the concurrent γ-ray and radio observations was to compare the γ-ray flux during giant pulses to that during weak pulses. Detecting the γ-ray flux during giant pulses required averaging many pulse periods of data. We generated a subaverage γ-ray profile that included only data from pulse periods in which the radio data displayed a giant pulse. To allow for the possibility of a delay between the radio and γ-ray effect, we also generated subaverages that included only data from pulse periods a fixed number of periods (n) away from radio bursts.

In order to select γ-ray data associated with each radio burst, we referenced both γ-ray and radio arrival times to the solar system barycenter. To remove the dispersion delay we shifted the radio times to infinite frequency. As a test of the barycenter correction and the clock synchronization, we compared radio and γ-ray arrival-time residuals for average profiles. After including a 2.042144 s offset in the *CGRO* clock, the 500 μs radio to gamma-ray offset was consistent with previous measurements. A similar test for the Vela pulsar confirmed the synchronization.

To determine the amount of enhancement of γ-ray flux during giant radio pulses, we compared the subaverage γ-ray profiles with a template profile made by including data from the entire 7 day observation. Figure 12 shows the template profile $x(\phi)$ and the subaverage profile $y_0(\phi)$. Each subaverage includes $\sim$2 minutes of data ($\sim$3600 pulse periods). We made the profile comparisons by performing linear least-squares fits of the scaled template to the subaverage profiles. We parameterized the fit as $y_n(\phi) = A + Bx(\phi)$, where B gives the ratio of pulsed flux in the two profiles $y_n(\phi)$ and $x(\phi)$ and A is the difference in background levels between y_n and x.

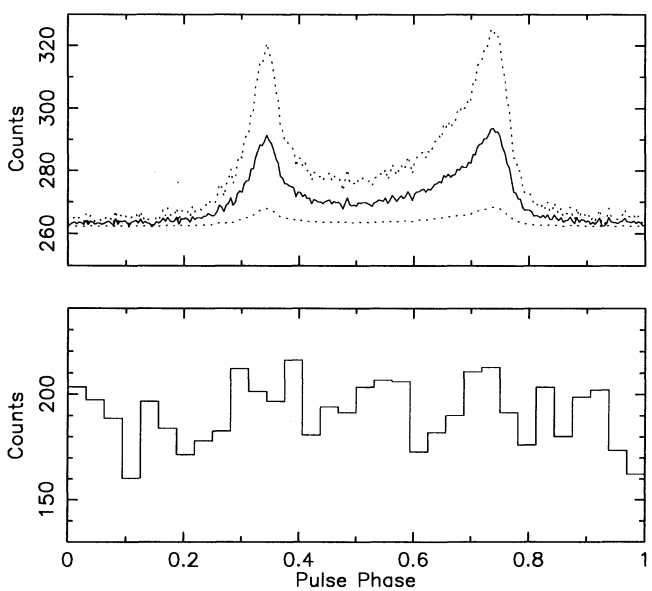

FIG. 12.—OSSE γ-ray pulse profiles for the Crab pulsar. The upper profile is calculated including all 7 days of data. The dotted lines indicate the $\pm 4\ \sigma$ range of increase or decrease in the average flux calculated during giant-pulse times. The lower plot is the subaverage profile that includes only data from giant pulse periods.

We considered a fit acceptable if the probability of getting a larger χ^2 is $>1\%$. A rejected fit would indicate that y_n is a different shape from x. For acceptable fits, limits on the deviations of the subaverage pulse amplitudes from the template profile are set by the confidence intervals on B. Applying this prescription to profiles y_n (for $-5 \le n \le 5$), all fits to $A + Bx$ fall within the acceptable range.

Figure 13 shows the scale factor B with 1 σ errors and the χ^2 of each fit for 30 degrees of freedom. Each average profile y_n yields a B that varies no more than a factor of 2.5 from unity, with a 95% confidence level. A value $B = 1$ implies no significant difference between the γ-ray profile during giant pulses and during weak pulses. We conclude that this test rules out variations larger than 2.5 times the average flux in γ-rays correlated with giant radio pulses.

The test considers only average γ-ray flux variability, where the average is over 2 minutes worth of pulse periods (3600 periods). If the γ-ray flux increased significantly during radio bursts (e.g., a factor of 10), but for only 10% of giant pulses, it would still be undetectable. Similarly, the flux could increase by a factor of 100 for only 1% of giant pulses and not be detected. Such effects would be observable in a histogram of single-pulse flux densities (as in § 5.1.1). However, the 100% fluctuations in the background level on a timescale of tens of minutes in OSSE data (caused by the orbit passing near the South Atlantic Anomaly) and the large error in estimating this background in a short time span combined with the low count rate from the pulsar itself make such a study impossible.

Lack of γ-ray fluctuations implies that the average pair-creation rate during and within five periods of giant radio bursts stays within 2.5 times the overall average rate. Probing variations below our 2.5 upper limit requires more data or a more sensitive γ-ray detector. However, this limit is enough to determine that radio fluctuations are primarily due to enhanced coherence. Enhanced pair creation, if it happens at

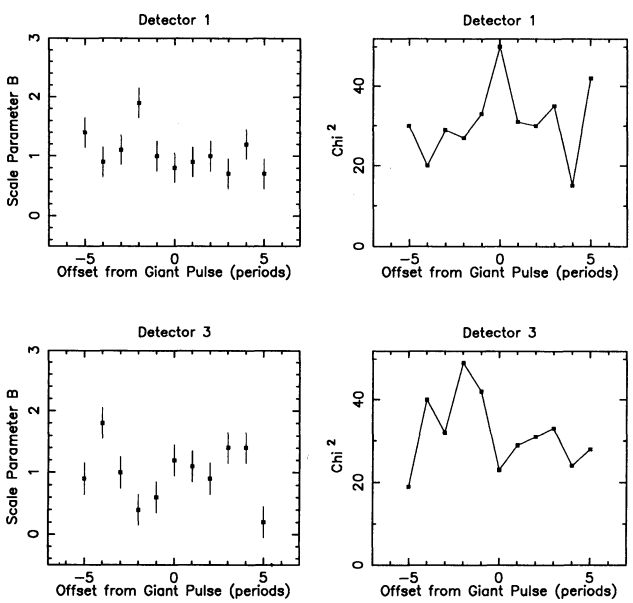

FIG. 13.—Plots of the flux ratio (B) of the average of γ-ray flux near giant-pulse times to the all-pulse average and estimates of χ^2 for the fit of giant-pulse profiles to all-pulse profiles with 30 degrees of freedom. Giant-pulse profiles were calculated for giant-pulse times as well as for pulses preceding or following giant pulses by up to five periods. Detectors 1 and 3 alternated looking at the Crab every 2 minutes, so the averages include different time periods for the two detectors.

all, is a small effect. The next section discusses these conclusions in more detail.

8. THEORETICAL IMPLICATIONS OF LACK OF γ-RAY/RADIO CORRELATIONS

Models for pulsar emission have been evolving over the past 20 years (e.g., Ruderman & Sutherland 1975; Arons 1981, Cheng, Ho, & Ruderman 1986). We focus on features of models in the literature tested by our observations. In particular, we interpret the lack of correlation between radio and γ-ray emission, considering only general features of all pulsar-emission models such as coherent radio emission, pair production, relativistic particle outflow, inverse-Compton scattering, and curvature radiation.

8.1. *Incoherent versus Coherent Effects and Pair-Production Rate Fluctuations*

There is no doubt that radio emission from pulsars comes from a coherent emission process (Cordes 1981) through particle-bunching or antenna mechanisms (Ruderman & Sutherland 1975; Cheng & Ruderman 1977; Buschauer & Benford 1980; Buschauer & Benford 1977; Michel 1987) or maser mechanisms (Asseo, Pellat, & Rosado 1980; Asseo, Pelletier, & Sol 1990; Luo & Melrose 1992). However, the role of coherence in causing flux variability remains unclear. Variability could be caused by changes in the number of emitting regions incoherently summed or by changes in the amount of coherence within a single emission region. In addition to uncertainty about coherence versus incoherence, further questions persist about the significance of variations in pair-production rate. For example, surface-temperature modulations could lead to modulation of outflowing particle fluxes, thus changing the flux of radiation as well (Cheng 1981). Examination of the radio-flux properties of giant pulses and comparison of radio-flux variation with γ-ray flux distinguishes the role of changes in coherence and changes in incoherent sums and constrains the amount of fluctuation in the pair-production rate.

Two effects could induce radio variability. In one scenario, a plasma-density fluctuation grows to encompass more particles within a single coherently emitting region. In this case, the flux scales as the square of the increase in plasma density. Ten times the normal density produces 100 times the flux, comparable to the amount of radio flux variability observed. An alternative model proposes increased radio flux due to an increased number of separate coherently emitting regions (like an array of coherent antennas). The large size of the whole region results in narrowband emission. If the independent regions are summed incoherently, the flux scales as simply the number of emitting regions.

Large particle-flow variations on timescales from 10 μs (gap discharge time) to the spin period (light-travel time to the light cylinder), as discussed by Arons (1979), are not permitted by the steady γ-ray flux. If flow variability is associated with the radio burst phenomenon, the factor of 2.5 upper limit on γ-ray flux variability limits any changes in flow to the same order of magnitude as the average flow. For a single emission region, lack of variation in the γ-ray flux requires any density enhancement by more than a factor of 2.5 to arise from rearrangement of existing plasma, as opposed to introduction of new particles by increase in the pair-production rate. Additional particle flow would inevitably create more curvature radiation in γ-rays, as the particles move out of the magnetosphere on curved field lines, in contradiction to observations. Similarly for an ensemble of emission sites, the new regions of emission added to the ensemble must come from redistribution of existing plasma flow, not enhanced flow.

The distribution of observed amplitudes of radio bursts (§ 5.1) indicates extreme time variability of the plasma instabilities creating the conditions for coherent emission. For an ensemble of emission regions, the power-law p.d.f. in the giant-pulse amplitude could result from a power-law p.d.f. in the number of emitting regions in the ensemble (ensemble size). A power-law p.d.f. in the ensemble size is impossible to produce for a fixed probability for the generation of a single bunch. In order to generate a power-law distribution of number of regions, the probability for generating a single coherent region must vary by orders of magnitude on a timescale of one period. During some periods, hundreds of bunches form. In other periods, none are present. Perhaps the probability for more bunches to form is enhanced by the number of bunches already present. On the other hand, a power-law p.d.f. for the number of particles within a single emitting region could naturally result from the nonlinearity of the bunch production mechanism in the plasma. Coherence combines with the power-law p.d.f. of ensemble size or number of particles to boost an order-of-magnitude effect in density to several orders of magnitude in flux. Perhaps the rate of giant pulses results from competition between the growth rate of plasma instabilities and turbulence in the magnetosphere that destroys the coherence built up by the instabilities.

Perhaps the best answer lies in a combination of both effects. The largest giant bursts are a sum of a large ensemble of particularly dense coherently emitting regions. The smaller giant pulses are formed by a smaller number of less dense emission regions. In any case, lack of enhanced γ-ray emission constrains particle flow variation associated with giant pulses to and increase of less than a factor of 2.5. The only way enhanced pair creation can play a significant role in the giant pulses is if the enhancement occurs for only a small ($< 1\%$) fraction of the overall particle outflow.

8.2. *γ-Ray Constraints on Inverse-Compton Scattering and Particle Populations*

Most pulsar γ-ray emission arises from curvature and synchrotron radiation of ultrarelativistic electrons. However, a fraction comes from inverse-Compton scattering (ICS) of lower energy photons by counterstreaming particles. Upper limits on γ-ray enhancement during giant radio bursts limit the energy distribution of particles available for ICS of the radio photons. Since no enhancement of γ-ray flux is observed during giant radio bursts, the fraction of γ-ray emission due to ICS of radio photons is limited to 1.5% when giant bursts are off. Then the increase in this fraction to 60% during giant bursts (number of γ-ray photons from ICS of radio photons should scale with radio flux density) would still be within the limits of γ-ray variability measured.

The fraction of γ-ray photons from ICS of radio photons places limits on the energy distribution of pairs accelerated in the magnetospheric gaps. For a radio photon to be scattered up to γ-ray energies requires scattering off an electron with $\gamma = 3 \times 10^5$. Alternatively, two collisions with $\gamma = 500$ electrons or three collisions with $\gamma = 70$ electrons will boost radio to γ-ray photons. In order to get the γ^2 boost with each inverse-Compton scattering event, the photon must change direction at each scattering (e.g., Rybicki & Lightman, p. 195). It alter-

nates scattering with the outward- and inward-streaming particles. The lower energy particles are far more common than high-energy particles because of the cascade of pair creation (Ruderman 1981). There are 10^4 pairs with $\gamma \sim 20$ produced by each high-energy particle ($\gamma = 2000$) outside the accelerating region. Although another simulation (Daugherty & Harding 1982) estimates only 10^2 pairs with $\gamma \sim 20$, it still predicts an energy distribution scaling as γ^2. The substantially larger number of low-energy particles compensates somewhat for the decreased probability of multiple scattering.

We now place limits on the high-energy particle distributions. From the measured flux densities and estimated distance, we calculate that there are about $n_\gamma \sim 10^{27}$ s^{-1} γ-ray photons (10^{36} ergs s^{-1}) and $n_r \sim 10^{35}$ s^{-1} radio photons (10^{31} ergs s^{-1}) on average. If the giant bursts are wideband, extending below $\nu \sim 100$ MHz where most of the radio photons are, the average burst contains $\sim 10^{37}$ s^{-1} radio photons. The largest bursts contain even more. The pair-production rate is estimated to be $\sim 10^{39}$ pairs s^{-1} (Arons 1981).

Since γ-ray flux increases by at most a factor of 2.5 during giant bursts, only $n_r/n_\gamma = 10^{-10}$ of burst photons can undergo ICS. This provides the limit $p_i(\gamma > E_i) < 10^{-10}$ on the probability for multiple ICS events [with $p_i(\gamma > E_i)$ defined as the probability for i ICS events with a particle of $\gamma > E_i$ and $E_1 = 3 \times 10^5$, $E_2 = 500$, $E_3 = 70$, and $E_4 = 25$].

Since $p_i = p_1^i$, we find

$$p_1(\gamma > 500) < 10^{-5}, \quad (10)$$

$$p_1(\gamma > 70) < 10^{-3.3}, \quad (11)$$

$$p_1(\gamma > 25) < 10^{-2.5}. \quad (12)$$

In order to convert these limits to particle energy distributions we need to consider the energy dependence of the ICS cross section. For all of the intermediate photons considered, the condition for Thomson scattering in the rest frame of the electron ($\gamma E \ll mc^2$) is satisfied (Rybicki & Lightman, p. 195). Thus the cross section is independent of energy. Because of the strong magnetic field, the cross section is actually dependent on the component of electron velocity perpendicular to the field (Blandford & Scharlemann 1976). However, we will assume that a substantial fraction of the secondary pairs is formed with large enough transverse motion and that they will retain it for long enough to lose some of their energy to inverse-Compton scattering. For cross section independent of energy, the limiting particle spectrum is proportional to the above probability for single scatterings. Namely, $n(E) \propto E^{-1}$. This falls between the slopes of the distribution function estimated by Arons (1981) in a pair-creation cascade model. For high-energy particles created by curvature γ-rays, $n(E) \propto E^{-4/15}$, and for lower energy particles created by synchrotron photons, $n(E) \propto E^{-3/2}$.

An upper limit on the fraction of radio photons scattered once by low-energy electrons could be measured by looking at the spectrum of single giant pulses from low to high radio frequencies. ICS could produce a measurable flux of 10 GHz and infrared photons from the giant bursts at 100 MHz, if induced scattering (in which the rate is enhanced in proportion to photon energy state occupation number) is significant (Blandford & Scharlemann 1976). Almost 1% of the 100 MHz radio flux could be shifted to higher frequencies. Measurement of this inverse-Compton tail on the radio spectrum of giant pulses would allow an extrapolation of the expected variability at optical through γ-ray frequencies due to inverse-Compton scattering of giant bursts in the radio. However, it may be difficult to separate the intrinsic width of the giant-burst spectrum from the inverse-Compton tail.

9. SUMMARY AND CONCLUSIONS

We have examined the timing, flux density, beaming, and occurrence rate of giant radio bursts from the Crab pulsar at 800 MHz. The Crab giant pulses are unique in the large dynamic range of their intensity fluctuations. The individual-pulse flux-density distribution is best fitted by a two-component model. The giant pulses make up 2.5% of all pulses and fall on a power law with index 3.3 and low flux density cutoff at 50 Jy. The remaining 97.5% of the pulses have a narrow distribution (spread < 1.5 Jy) centered at 1.5 Jy. Such a model suggests that giant pulses are formed by a distinct mechanism rather than simply an extrapolation of a weak-pulse flux-density distribution.

By measuring timescales and sizes of giant pulses, we have constrained temporal and angular properties in the magnetosphere. The observed single-pulse width of 100 ± 50 μs places a lower limit on both the angular width of the beam and the duration of the bursts. The envelope of the arrival time residuals and the 250 μs width of the average profile places an upper limit of 100 μs on the beam width, after taking into account the 300 μs sample interval. The small envelope rules out a wavering steady-beam model for giant pulses. The maximum angle of waver from the line of sight is too small to produce the small fraction of pulses observed as giant.

Temporal modulation was demonstrated to be the best explanation for giant bursts. Since the number of giant pulses separated by one period is consistent with the expectation for a Poisson process, the burst duration is limited to less than one period. Further indication of the short duration comes from the lack of correlation between giant pulses and either the previous-pulse flux density or the next-pulse flux density. Apparently, each giant pulse is caused by a single, short-timescale enhancement that disappears in a time shorter than the timescale for particle flow out of the magnetosphere. From the rate of giant pulses and Poisson statistics, we find the average time separation between giant pulses, $t_{\rm sep} = (430 \pm 50)t_{\rm hi}$ for giant pulses above 125 Jy or $t_{\rm sep} = (40 \pm 3)t_{\rm hi}$ for giant pulses above 50 Jy. Day-to-day variability in the observed rate of giant pulses above a fixed threshold is due to refractive interstellar scintillations, *not* intrinsic variation at the pulsar.

In our timing analysis we find no offset between giant-pulse and average-pulse arrival times. Both using individual giant-pulse arrival times and forming a giant-pulse subaverage profile, we find an offset of 6 ± 12 μs from the average-pulse arrival time, consistent with no offset. No offset implies that while giant pulses may form from a different mechanism than weaker pulses, the mechanism must operate at the same location in the magnetosphere as the mechanism for weaker pulses.

The correlation analysis between the γ-ray and radio observations reveals that the γ-ray emission does not vary more than 2.5 times the average level at the giant radio-burst times. Lack of correlation implies that giant radio bursts are primarily caused by enhanced coherence, not variable pair-creation rates.

While this work has put some constraints on pulsar emission mechanisms in both radio and γ-rays, further observations are necessary to clearly distinguish competing models. We propose several new observations which have a high probability of

providing new insight into the major uncertainties yet to be resolved.

Radio observations need improvement in three areas: time resolution, bandwidth coverage, and sensitivity. High time resolution observations, which also require more frequency channels to reduce the dispersion smearing per channel, will resolve the fine structure of giant pulses. In particular, examination of the edges of the beam will disentangle duration effects from angular size effects on the observed profile. Simultaneous observations at multiple radio frequencies will determine the correlation bandwidth of giant pulses and display scaling of width and arrival times with frequency. The wideband spectrum of individual giant pulses will indicate the significance of inverse-Compton scattering determined by the energy distribution of relativistic particles in the magnetosphere.

Because of the Crab Nebula background, only the strongest 10% of the giant pulses are detectable above the noise at Green Bank. VLA observations resolve out 90% of the nebula and hence probe the low flux-density part of the giant-pulse distribution. In addition, the next generation γ-ray telescope will provide enough sensitivity to probe smaller fluctuations in a shorter time span. Such short-timescale variability studies will allow tests of models not only in their average behavior but also in their detailed microphysics. In the nearer future, correlation studies with higher energy γ-rays using data from the *CGRO* Energetic Gamma-Ray Experiment Telescope (EGRET) (Fierro et al. 1993), as well as TeV γ-rays observed from Whipple Observatory (Reynolds et al. 1993), will provide insight into the most energetic phenomena in pulsar magnetospheres. These are particularly intriguing projects given the long-timescale changes in γ-ray flux detected at low significance (Nolan et al. 1993).

While significant progress has been made recently in understanding pulsar emission mechanisms, much remains to be clarified. Most of the recent progress has emerged from the analysis of new γ-ray data. However, only through multiwavelength studies from radio through γ-rays can we form a complete picture of pulsar magnetospheric physics.

Many people worked together to make this project possible. We appreciate the cooperation of James Kurfess and the rest of the OSSE team in making the joint observations possible. We would especially like to thank NSF REU student Chris Garasi for his initial work developing software for radio data reduction. We found helpful the comments on earlier versions of the manuscript from the anonymous referee, Jean Eilek, James Weatherall, and Stephen Thorsett. The staff at the Green Bank Observatory made a special effort to assure a successful observing run for this project. Rick Fisher and Mark Clark were particularly helpful in accommodating our unusual use of their data acquisition system. Green Bank Observatory is part of the National Radio Astronomy Observatory, which is operated by Associated Universities, Inc. under cooperative agreement with the National Science Foundation (NSF). The Arecibo Observatory is part of the National Astronomy and Ionosphere Center, which is operated by Cornell University under cooperative agreement with NSF. Observations at the Palomar Observatory were made as part of a continuing collaborative agreement between the California Institute of Technology and Cornell University. This research was funded by NASA grants NAG 5-1452, NAG 5-2436, DPR S-10987C, and NSF grant AST 92-18075. Basic research in precision pulsar astrophysics at the Naval Research Laboratory is supported by the Office of Naval Research.

REFERENCES

Argyle, E. 1973, ApJ, 183, 973
Argyle, E., & Gower, J. F. R. 1974, ApJ, 175, L89
Arons, J. 1979, Space Sci. Rev., 24, 437
———. 1981, in IAU Symp. 95, Pulsars, ed. W. Sieber & R. Wielebinski (Dordrecht: Reidel), 69
Asseo, E., Pellat, R., & Rosado, M. 1980, ApJ, 239, 661
Asseo, E., Pelletier, G., & Sol, H. 1990, ApJ, 247, 529
Backer, D. C. 1971, Ph.D. thesis, Cornell Univ.
———. 1973, ApJ, 182, 245
Bartel, N., Sieber, W., & Wolszczan, A. 1980, A&A, 90, 58
Biggs, J. D. 1986, Ph.D. thesis, Univ. of Sydney
Blandford, R. D., & Scharlemann, E. T. 1976, MNRAS, 174, 59
Buschauer, R., & Benford, G. 1977, ApJ, 179, 189
———. 1980, ApJ, 190, 945
Cheng, A. F. 1981, in IAU Symp. 95, Pulsars, ed. W. Sieber & R. Wielebinski (Dordrecht: Reidel), 99
Cheng, A. F., & Ruderman, M. A. 1977, ApJ, 212, 800
Cheng, K. S., Ho, C., & Ruderman, M. 1986, ApJ, 300, 500
Cordes, J. M. 1981, in IAU Symp. 95, Pulsars, ed. W. Sieber & R. Wielebinski (Dordrecht: Reidel), 115
Cordes, J. M., Weisberg, J. M., & Boriakoff, V. 1985, ApJ, 228, 221
Counselman, C. C., & Rankin, J. M. 1971, ApJ, 166, 513
Daugherty, J. K., & Harding, A. K. 1982, ApJ, 252, 337
Deich, W. T. S., Cordes, J. M., Hankins, T. H., & Rankin, J. M. 1986, ApJ, 300, 540
Fierro, J. M., et al. 1993, in Proc. of the Compton Gamma Ray Symposium, ed. J. Norris (College Park, MD: NASA), in press
Friedman, J. F., & Boriakoff, V. 1990, in Proc. IAU Colloq. 128, Magnetospheric Structure and Emission Mechanisms of Radio Pulsars, ed. T. H. Hankins, J. M. Rankin, & J. A. Gil (Poland: Pedagogical University Press), 347
Gower, J. F. R., & Argyle, E. 1972, ApJ, 171, L23
Hankins, T. H. 1993, BAAS, 24, 1277
Hankins, T. H., & Rickett, B. J. 1975, Meth. Comput. Phys., 14, 55
Hegyi, D., Novick, R., & Thaddeus, P. 1971, in IAU Symp. 46, The Crab Nebula, ed. R. D. Davies & F. G. Smith (Dordrecht: Reidel), 129
Heiles, C., Campbell, D., & Rankin, J. 1970, Nature, 226, 529
Hesse, K. H., & Wielebinski, R. 1974, A&A, 31, 409
Isaacman, R., & Rankin, J. M. 1977, ApJ, 214, 214
Johnson, W. N., et al. 1989, in Proc. Gamma Ray Observatory Science Workshop, ed. N. Johnson (Greenbelt: NASA), 2
Lundgren, S. C. 1994, Ph.D. thesis, Cornell Univ.
Lundgren, S. C., Cordes, J. M., & Beckwith, S. V. W. 1995, ApJ, submitted
Luo, Q., & Melrose, D. B. 1992, MNRAS, 258, 616
Lyne, A. G., & Thorn, D. J. 1975, MNRAS, 172, 97
Michel, F. C. 1987, ApJ, 322, 822
Nolan, P. L., et al. 1993, ApJ, 409, 697
Percival, J. W., et al. 1993, ApJ, 407, 276
Reynolds, P. T., et al. 1993, ApJ, 404, 206
Rickett, B., & Lyne, A. G. 1990, MNRAS, 224, 68
Ritchings, R. T. 1976, MNRAS, 176, 249
Ruderman, M. 1981, in IAU Symp. 95, Pulsars, ed. W. Sieber & R. Wielebinski (Dordrecht: Reidel), 87
Ruderman, M. A., & Sutherland, P. G. 1975, ApJ, 196, 51
Rybicki, G. B., & Lightman, A. P. 1979, Radiative Processes in Astrophysics (New York: John Wiley & Sons)
Staelin, D. H., & Sutton, J. M. 1970, Nature, 228, 69
Taylor, J. H., Manchester, R. N., & Lyne, A. G. 1993, ApJS, 88, 529
Taylor, J. H., & Weisberg, J. 1989, ApJ, 345, 434
Ulmer, M. P., et al. 1991, in The Compton Observatory Science Workshop, ed. C. R. Shrader, N. Gehrels, & B. Dennis (NASA Conf. Pub. 3137) (Washington: NASA), 253
Weisberg, J., et al. 1986, AJ, 92, 621